



High-temperature stability of retained austenite and plastic deformation mechanism of ultra-fine bainitic steel isothermally treated below M_s

Ting-ting He^{1,2} · Feng Hu^{1,2} · Kun Wang^{1,2} · Wen Zhou^{1,2} · Li Li³ · Serhii Yershov^{1,2} · Kai-ming Wu^{1,2}

Received: 11 August 2023 / Revised: 22 November 2023 / Accepted: 24 November 2023 / Published online: 1 April 2024
© China Iron and Steel Research Institute Group Co., Ltd. 2024

Abstract

The mechanical properties of the sample and the stability of retained austenite were studied by designing two kinds of ultra-fine bainitic steel with different heat treatment methods (austempering above and below M_s (martensite start temperature)), which were subjected to tensile tests at 20 and 450 °C, respectively. The results show that compared to room temperature (20 °C) tensile properties, the uniform elongation of the sample at high temperature (450 °C) significantly decreased. Specifically, the uniform elongation of the sample austempered above M_s decreased from 8.0% to 3.5%, and the sample austempered below M_s decreased from 10.9% to 3.1%. Additionally, the tensile strength of the sample austempered above M_s significantly decreased (from 1281 to 912 MPa), and the sample austempered below M_s slightly decreased (from 1010 to 974 MPa). This was due to the high carbon content (1.60 wt.%), high mechanical stability, low thermal stability for the retained austenite of the sample austempered below M_s . Besides, the retained austenite decomposed at high temperatures, the carbon content and transformation driving force were significantly reduced, the transformation rate increased, and the phase transformation content reduced.

Keywords Ultra-fine bainite · Isothermal treatment · High-temperature tensile property · Retained austenite stability · Plastic deformation

1 Introduction

Ultra-fine bainitic steel with excellent mechanical properties has become a typical representative of the new-generation advanced high-strength steel, widely used in bearing [1] and the automotive industry [2]. Bearing and automotive steel must consider their high-temperature properties when used [3, 4] because their microstructure and mechanical properties may change at high

temperatures. Therefore, to ensure safety and stability in the service process, it is necessary to study the high-temperature mechanical properties of ultra-fine bainitic steel. As an important constituent phase in ultra-fine bainitic steels, the content and stability of retained austenite significantly affect the final mechanical properties of steel materials [5–10]. The retained austenite in bainitic steel belongs to the metastable phase, which undergoes martensite transformation due to the applied stress or strain, called the transformation-induced plasticity (TRIP) effect. The TRIP effect of retained austenite during the tensile process increases the strain-hardening rate of the materials and delay necking, thus improving the uniform elongation and strength of the materials [11–13]. Through in-depth research, it is found that the TRIP effect of bainitic steel during deformation is related to the content and stability of retained austenite. When the stability of retained austenite is too poor or too strong, it has a minor contribution to the strength and plastic properties of the material [14, 15].

✉ Feng Hu
hufeng@wust.edu.cn

¹ The State Key Laboratory of Refractories and Metallurgy, Wuhan University of Science and Technology, Wuhan 430081, Hubei, China

² Collaborative Innovation Center for Advanced Steels, Wuhan University of Science and Technology, Wuhan 430081, Hubei, China

³ Zhejiang Tsingshan Iron and Steel Co., Ltd., Qingtian 323903, Zhejiang, China

The main factors influencing the stability of retained austenite are temperature [16], chemical composition [17, 18], grain size [19–21], and stress state [22, 23], of which the most important is temperature. The temperature affects the stability mainly by the relationship between deformation and M'_s temperatures (starting temperature of martensitic transformation of the retained austenite). When the deformation temperature is lower than M'_s , the driving force for the transformation of retained austenite to martensite increases, and when the deformation temperature is higher than M'_s , the corresponding driving force decreases and the occurrence of martensite transformation requires greater external stress [24, 25]. Moreover, at high temperatures, the retained austenite may undergo decomposition, which occurs when film retained austenite first produces fine cementite precipitates, then block retained austenite generates fine cementite precipitates, and finally retained austenite decomposes into ferrite and cementite [26–29]. It effectively obtains retained austenite with high content and good stability to increase the TRIP effect and improve high-temperature mechanical properties of ultra-fine bainitic steel.

The strength and plasticity of ultra-fine bainitic steel can be improved by metastable retained austenite transformation to martensite during tensile deformation. However, due to morphology, size, content, carbon content, and stability differences, the transformation behavior of film and block retained austenite in the high-temperature tensile process differs, and the improvement effect on strength and plasticity is also different [30–32]. Relevant literature [8, 11] and the authors' group [10, 33–35] have studied the mechanical properties of ultra-fine bainite at room temperatures and the TRIP effect during tensile deformation. However, the stability of retained austenite in the high-temperature tensile process and its plastic deformation mechanism must be further studied. Hence, this paper designed two kinds of ultra-fine bainitic steels with different heat treatment processes (austempering above M_s at 400 °C for 2 h and austempering below M_s at 300 °C for 8 h). Tensile tests were conducted at different temperatures (room temperature of 20 °C and high temperature of 450 °C) to further study the high-temperature mechanical properties of ultra-fine bainitic steel and explore the influence of two different forms of retained austenite on its deformation behavior at high temperatures. Meanwhile, the stability of retained austenite in ultra-fine bainitic steel and the transformation law in the high-temperature tensile process were studied by combining the work-hardening behavior and transformation thermodynamics and dynamics.

2 Materials and methods

The investigated steel with composition (wt.%) of C 0.3, Mn 1.52, Si 0.26, Cr 0.27, Ni 1.51, Al 1.10, Mo 0.25, 0.016 Nb, and Fe balance was cut into a round rod sample with a size of $\phi 6$ mm \times 70 mm and was used for thermal simulation test. Figure 1a and b illustrates the obtained thermal expansion curves, where the phase transformation temperatures A_{c1} , A_{c3} , M_s and M_f of the investigated steel are 742, 874, 354, and 204 °C, respectively. The TTT curve (isothermal transformation curve of under-cooled austenite) was drawn using J-MatPro, which provides a theoretical basis for the subsequent development of heat treatment processes for investigated steel. In order to obtain different microstructures, two types of heat treatment processes were determined. Samples were austenitized at 900 °C for 30 min in a box furnace, and then was transferred to a low-temperature box furnace. The samples were isothermally treated at 400 °C for 2 h (above M_s) and at 300 °C for 8 h (below M_s), respectively, and were named as Samples A and B. And finally, the samples were water cooled to room temperature.

According to the tensile experiment requirements, the gauge distance of the tensile sample was determined to be 25 mm, and the tensile rate was $6.7 \times 10^{-4} \text{ s}^{-1}$. Both investigated steels were subjected to tensile tests at 20 and 450 °C. In the tensile test at 450 °C, the temperature program was first set to rise on the MTS tensile test machine (heating for 30 min to 450 °C and holding for 15 min), and then, the test could be conducted. After the sample was broken, the area with the highest deformation of the broken sample was observed.

After observing the fracture surface of the sample, 4 vol.% nitric acid alcohol solution was used for corrosion after grinding and polishing, and the morphology was observed under an optical microscope (OM, Olympus) and scanning electron microscope (SEM, Nova 400 Nano). After the samples were electrolytically polished in 5 vol.% perchloric acid solution, the structure morphology and orientation were characterized using the electron backscatter diffraction (EBSD, JEOL-7600F). The working conditions for the EBSD analysis were as follows: acceleration voltage of 20 kV, inclination of 70°, step of 100 nm, and beam intensity of 13 nA.

The sample was ground to 40–80 μm , and a special punch was used to punch out a small disk of 3 mm in diameter. Additionally, an electrolytic double spray thinning (10% perchloric acid and 90% acetic acid) was applied on the MTP-1A electrolytic double spray tester, and the material's microstructure was analyzed using a transmission electron microscope (TEM, JEM-2010HT).

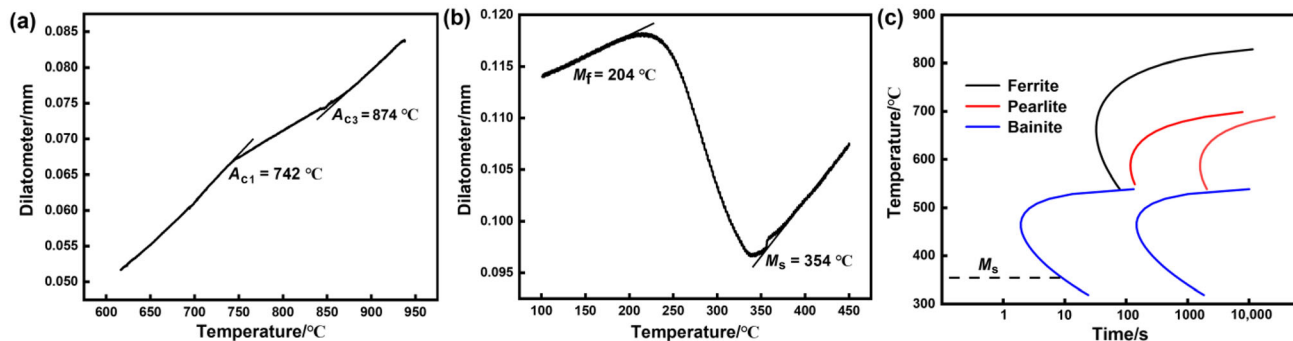


Fig. 1 Thermal expansion curves (a, b) and TTT simulation curve (c) of investigated steel

X-ray diffraction analysis (XRD, D8 Advance) was used to determine the fraction of retained austenite (V_γ) and its carbon content (w_C). After the sample was ground and mechanically polished, the surface stress was removed by electrolytic corrosion with 5 vol.% perchloric acid solution. Using Cu $K\alpha$ radiation, tube pressure was 40 kV, tube current was 45 mA, step length was 1 ($^\circ$)/min, and measurement angle ranged 20 $^\circ$ –110 $^\circ$. The volume fraction and carbon content of the retained austenite could be calculated as follows [36, 37]:

$$R = \left(\frac{1}{v^2}\right) \left[|F|^2 P \left(\frac{1 + \cos^2 2\theta}{\sin^2 \theta \cos \theta}\right)\right] (e^{-2M}) \tag{1}$$

$$V_\gamma = \frac{\frac{1}{m} \sum_{j=1}^m \frac{I_\gamma^j}{R_\gamma^j}}{\frac{1}{m} \sum_{j=1}^m \frac{I_\gamma^j}{R_\gamma^j} + \frac{1}{m} \sum_{j=1}^m \frac{I_\alpha^j}{R_\alpha^j}} \tag{2}$$

$$w_C = \frac{\alpha_\gamma - 3.547}{0.0467} \tag{3}$$

where v is the volume of unit cell; m is the number of examined peaks; F is the structural factor; P is the multiplicity factor; θ is semi-diffraction angle; R is the material scattering factor and depends on θ , interplanar spacing, composition and the crystal structure of the phase; R_γ and R_α are the scattering factor of γ phase and α phase, respectively; e^{-2M} is the temperature factor; $\frac{1 + \cos^2 2\theta}{\sin^2 \theta \cos \theta}$ is the angular factor (including polarization factor and Lorentz factor); I_α is the integral intensity of α diffraction peak; I_γ is the integral intensity of γ diffraction peak, in which the diffraction peaks of the (200) and (211) are selected for the bainite and martensite phases (α phase), and the (200), (220) and (311) diffraction peak are selected for the austenite phase (γ phase); and α_γ is the lattice constant of austenite.

3 Results

3.1 Mechanical properties

The engineering stress–strain curve (Eqs. (4) and (5)), true stress–strain curve (Eqs. (6) and (7)), and stress–strain-hardening rate curve of the investigated steel are shown in Fig. 2, and their strength and elongation are shown in Table 1. Compared to the room temperature tensile properties, the uniform elongation (uniform elongation refers to the percentage increase in the length of the material from the beginning of plastic deformation to the beginning of necking during tension, and the retained austenite produces martensitic transformation in this stage) of the sample under high temperature significantly decreases, while the changes in strength are different between the two kinds of samples. The uniform elongation and tensile strength of Sample A significantly decrease (the uniform elongation decreased from 8.0% to 3.5%, and the tensile strength decreased from 1281 to 912 MPa), but the total elongation increased significantly (from 13.3% to 20.9%). The change in uniform elongation of Sample B is the most significant (decreased from 10.9% to 3.1%), while the total elongation changed very little (from 22.0% to 19.8%), and the tensile strength slightly decreased (from 1010 to 974 MPa). In the high-temperature tensile process, the work-hardening rate of Sample B was significantly higher than that of Sample A. Simultaneously, the work-hardening stage of the sample at high temperatures was shorter, and necking was obvious.

$$\sigma_e = \frac{B}{A_0} \tag{4}$$

$$\varepsilon_e = \frac{d}{L_0} \tag{5}$$

$$\sigma_T = \sigma_e (1 + \varepsilon_e) \tag{6}$$

$$\varepsilon_T = \ln(1 + \varepsilon_e) \tag{7}$$

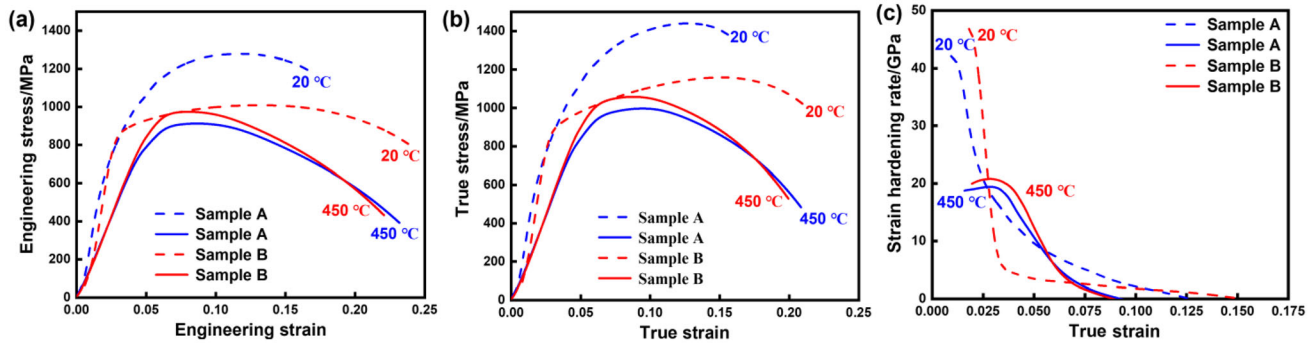


Fig. 2 Engineering stress–strain curve (a), true stress–strain curve (b), and strain-hardening rate (c) of investigated steel

Table 1 Tensile properties of investigated steel

Sample	Tensile temperature/°C	σ_y /MPa	σ_{UTS} /MPa	ε_T /%	ε_U /%
A	20	706	1281	13.3	8.0
	450	716	912	20.9	3.5
B	20	792	1010	22.0	10.9
	450	764	974	19.8	3.1

σ_y —Yield strength; σ_{UTS} —tensile strength; ε_T —true strain; ε_U —uniform elongation

where σ_e is engineering stress; ε_e engineering strain; B is the force applied; A_0 is the original cross-sectional area; d is the varying length; L_0 is the original length and σ_T is true stress.

3.2 Microstructure

Figure 3 depicts the OM and TEM structures of the investigated steel before tensile deformation. The microstructure of the sample includes block martensite–austenite (block M-RA), bainitic ferrite (BF), and film retained austenite (film RA), which is distributed between BF laths. The two (film RA and BF laths) are arranged in parallel. Martensite exists not only as block martensite–austenite but also as pre-martensite (PM) in Sample B. Compared with Sample A, Sample B has a smaller size and lower block M-RA content. The isothermal time is prolonged, the temperature decreases, and the microstructure is significantly refined. An important reason for microstructure refinement is that the order of phase formation of Sample B during heat treatment is pre-martensite, bainite, martensite, and pre-martensite can refine the bainite formed around it [38].

The SEM microstructure of the investigated steel before tensile deformation and after room temperature/high-temperature tensile deformation (after the tensile fracture deformation) is presented in Fig. 4. Before tensile deformation, the size and proportion of the block M-RA

structure of Sample B are smaller than those of Sample A, and the BF laths is also thinner. After tensile deformation, the microstructure of the investigated steel is deformed, the BF laths and block structure are elongated along the tensile direction, and cracks appear. The microstructure changes of Sample A under different temperatures stretching are significantly different. The microstructure deformation under the 450 °C tensile test is more obvious than that under the 20 °C tensile test. In contrast, the microstructure deformation of Sample B is very obvious under the 450 and 20 °C tensile conditions, with little difference.

Figure 5 illustrates the TEM microstructure of the investigated steel after high-temperature tensile deformation. After tensile deformation, the microstructure is retained austenite, martensite, and bainitic-ferrite, and part of the retained austenite (γ) undergoes martensite transformation (Fig. 5c, f). Through diffraction pattern calibration, it is determined that the strain-induced martensite is body-centered cubic (BCC) α' -martensite. Previous work [35] suggested that the sample undergoes martensite transformation in the tensile process at room temperatures, and the generated martensite is not only BCC martensite but also closely packed hexagonal (HCP) ε -martensite, and there is $\gamma \rightarrow \varepsilon \rightarrow \alpha'$ transformation mechanism.

Figure 6 presents the fracture morphology and microstructure of the investigated steel after tensile deformation. The two samples are ductile fractures at high temperatures. The dimples on the fracture surface are dense and deep, and the cracks are short, mainly in the form of

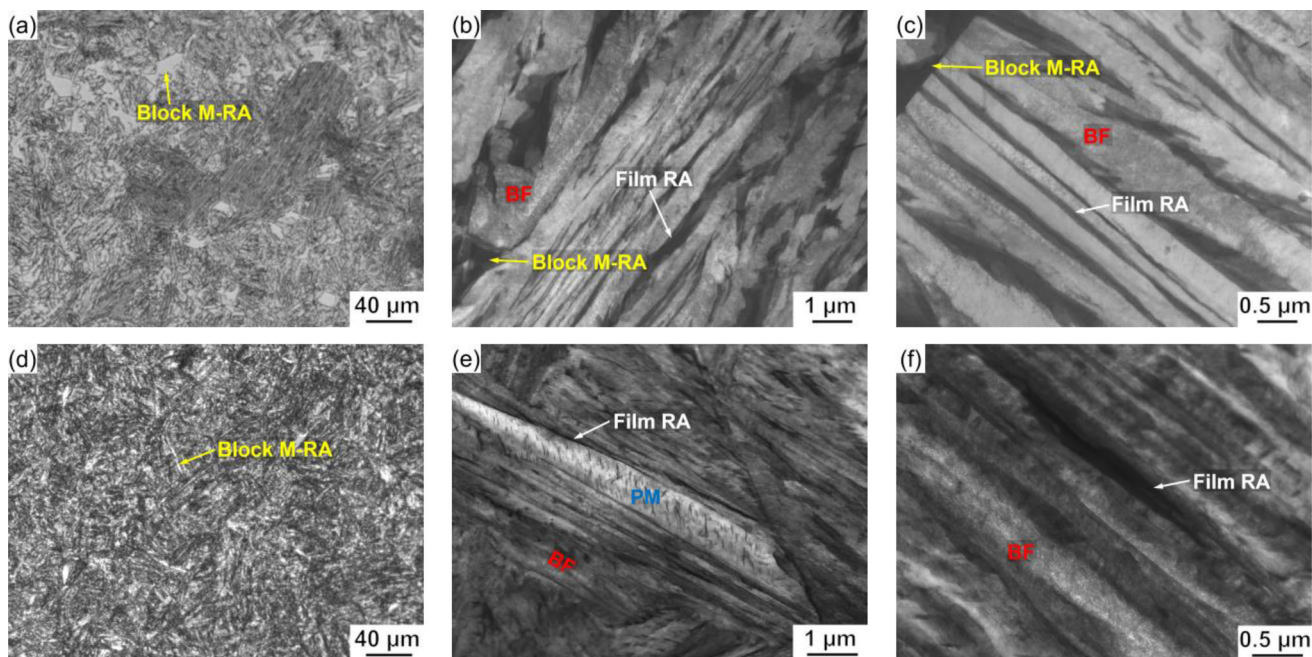


Fig. 3 OM and TEM micrographs of samples before tensile deformation in investigated steel. **a–c** Sample A; **d–f** Sample B

pores. The cleavage surface is obvious at the dimple. The fracture modes of the two samples are different at room temperatures. Sample A is brittle fracture, the cleavage surface is fluvial, and the crack is obvious. Sample B is ductile fracture, the dimple distribution is uniform and shallow, and the number of cracks is large and obvious. Compared with Sample A, the plastic difference of Sample B is smaller at different temperatures. The necking of the two samples is more obvious at high temperatures.

3.3 EBSD characterization

The inverse pole figure (IPF) in EBSD of the investigated steel is shown in Fig. 7, and the effective grain size statistics diagram and statistical results are presented in Fig. 8a, d, and Table 2, respectively. Different colors represent different grain orientations, and similar colors represent the same or similar crystallography orientations in the IPF diagram. The effective grain size is calculated based on the EBSD results, and the grain size is calculated

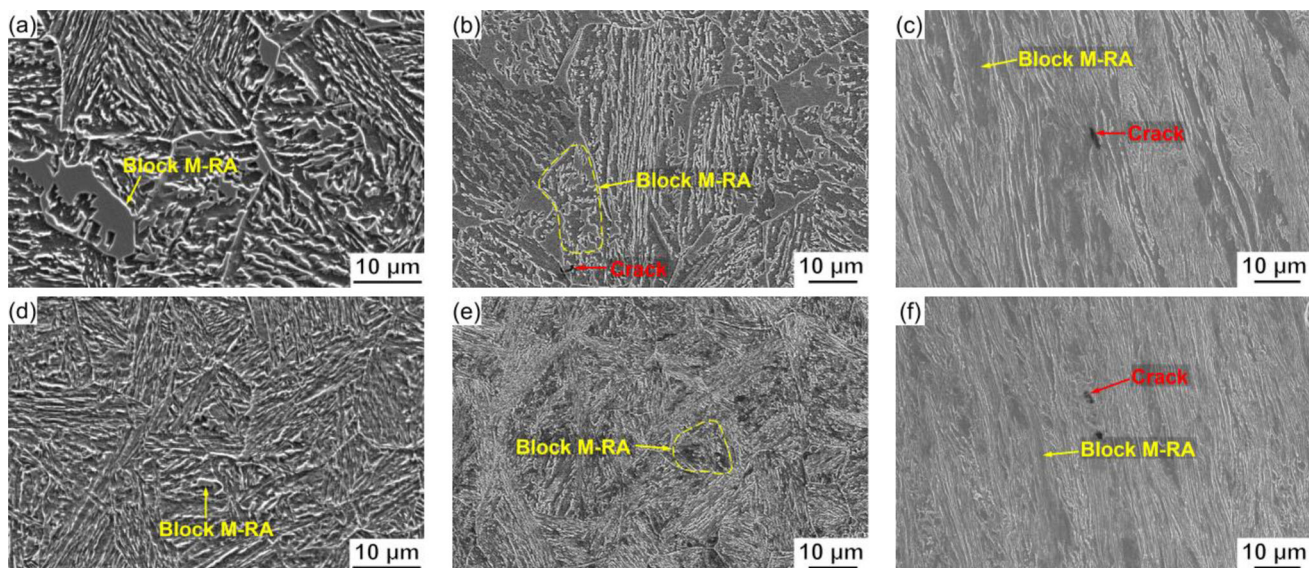


Fig. 4 SEM micrographs of Sample A (**a–c**) and Sample B (**d–f**). **a, d** Before tensile deformation; **b, e** after tensile deformation at 20 °C; **c, f** after tensile deformation at 450 °C

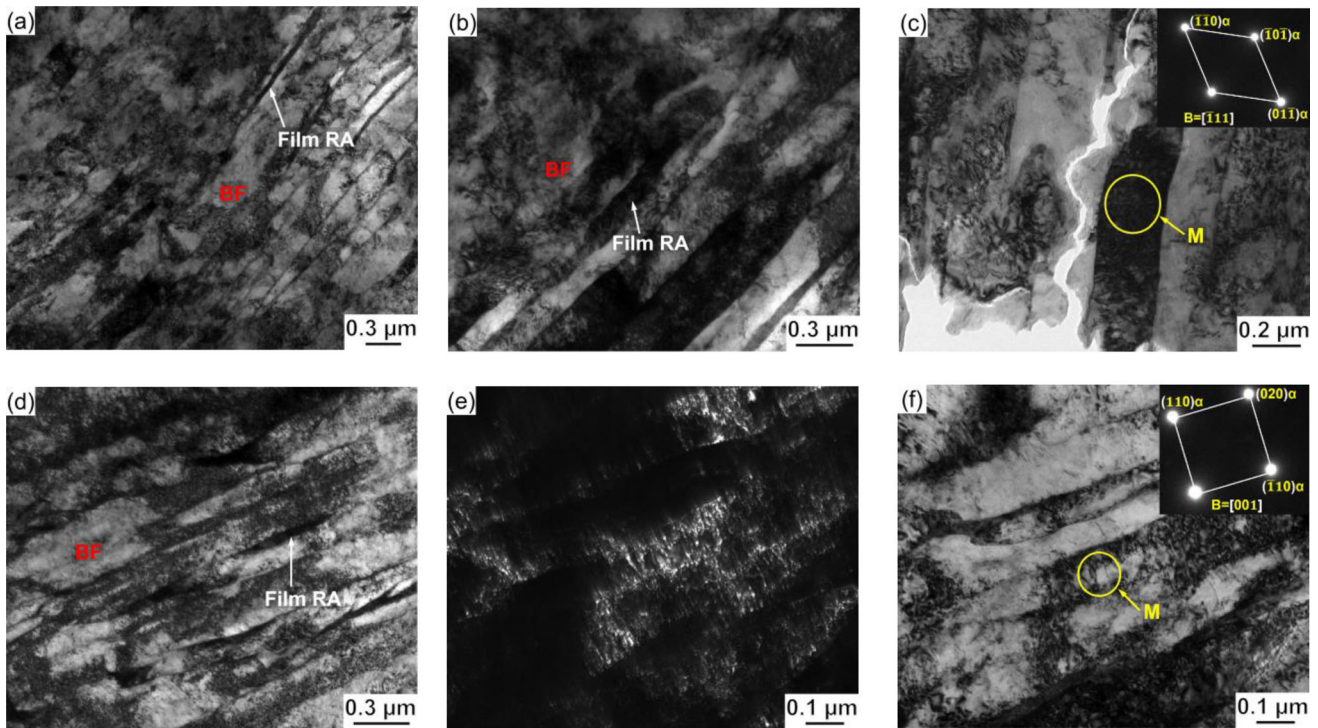


Fig. 5 TEM micrographs of investigated steel after tensile deformation at 450 °C. a–c Sample A; d–f Sample B

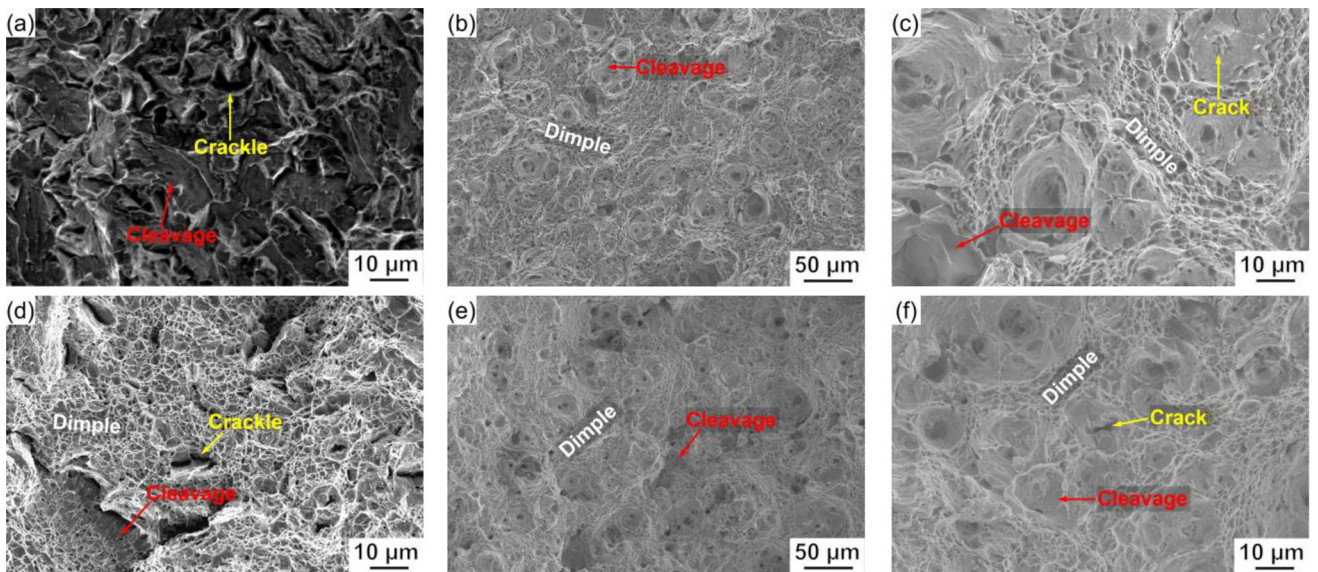


Fig. 6 Fracture morphology of Sample A (a–c) and Sample B (d–f). a, d After tensile deformation at 20 °C; b, c, e, f after tensile deformation at 450 °C

according to the equivalent circular diameter. The effective grain size of the sample significantly decreased after tensile deformation. Compared to the change in effective grain size under the 20 °C tensile test (the effective grain size decreased from 1.1 to 0.7 μm of Sample A and from 1.3 to 0.5 μm of Sample B), the change in effective grain size of Sample A under the 450 °C tensile test was greater (the

effective grain size decreased from 1.1 to 0.5 μm). The change in effective grain size of the Sample B under the 450 °C tensile test was smaller (the effective grain size decreased from 1.3 to 0.6 μm). The change in effective grain size of Sample B under tensile conditions at different temperatures is more significant than that of Sample A.

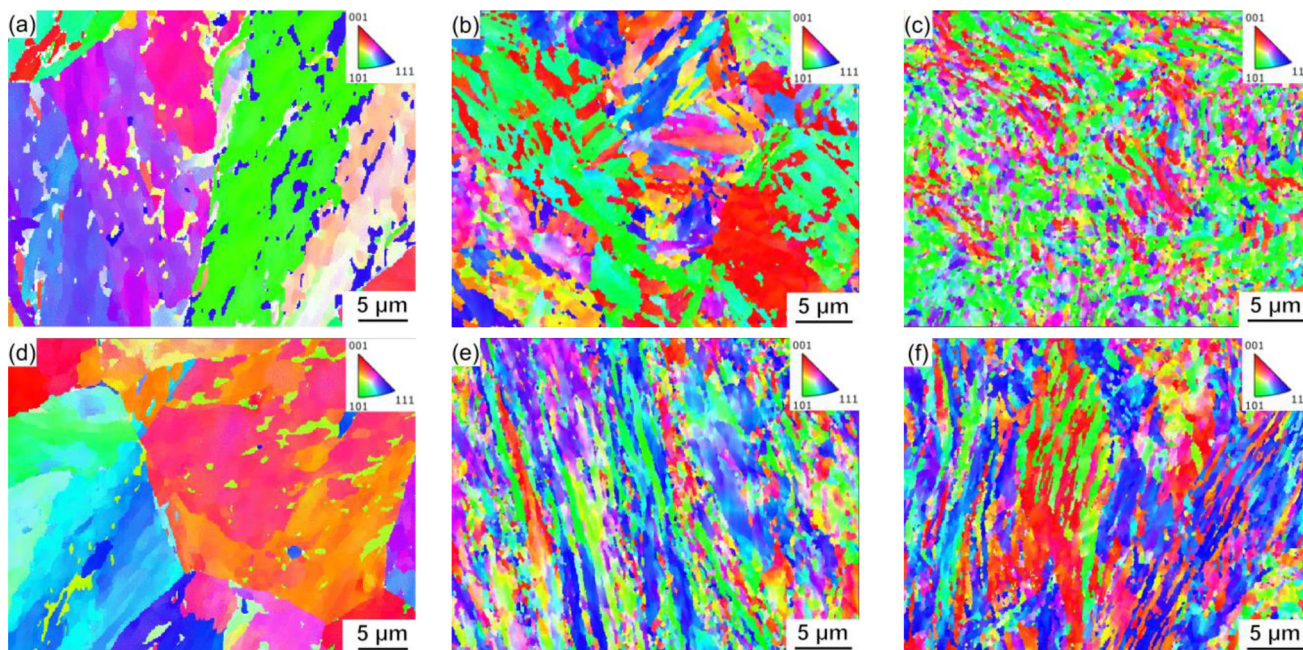


Fig. 7 EBSD micrographs (IPF) for Sample A (a–c) and Sample B (d–f). **a, d** Before tensile deformation; **b, e** after tensile deformation at 20 °C; **c, f** after tensile deformation at 450 °C

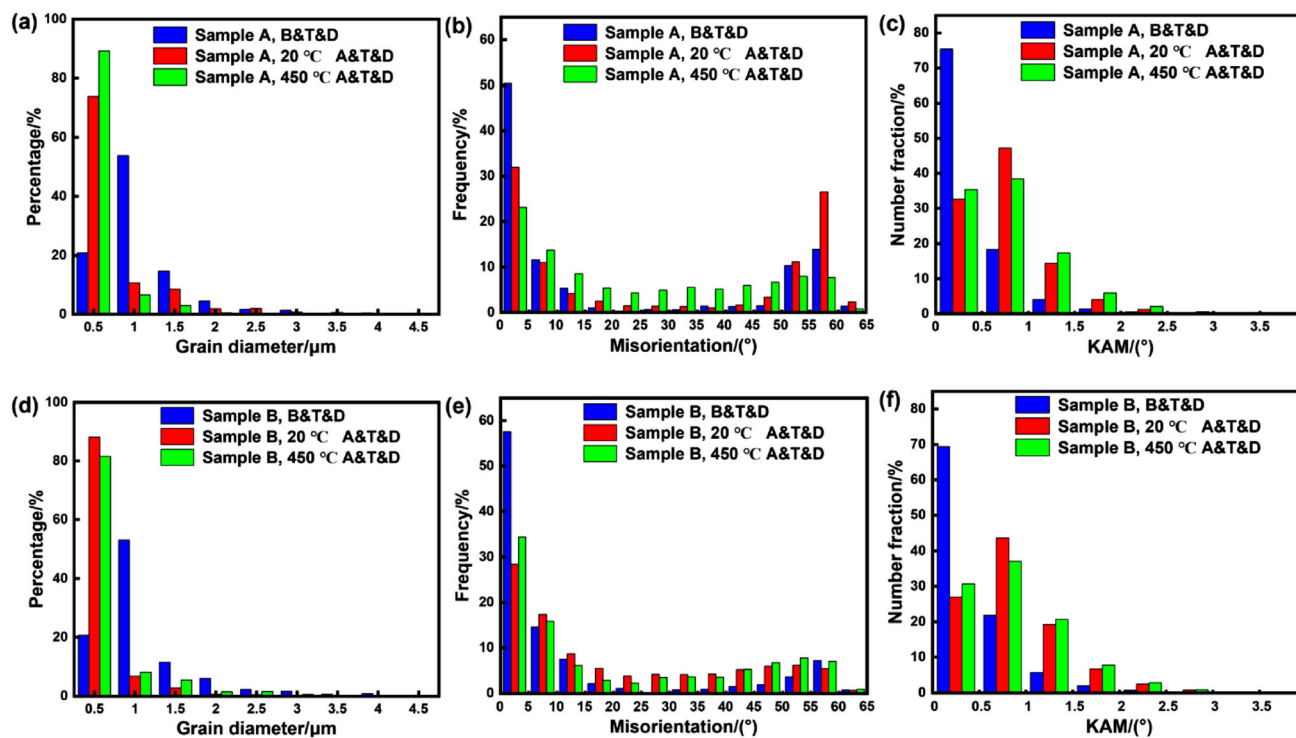


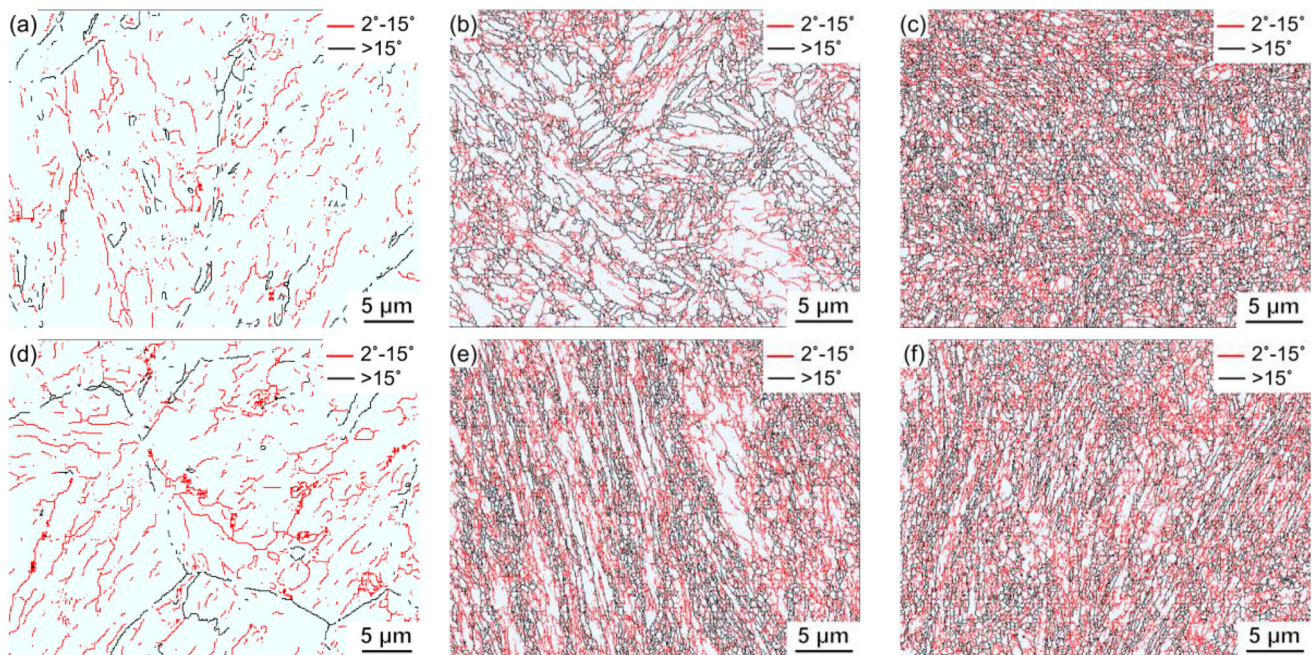
Fig. 8 Statistical diagram of effective grain size (**a, d**), statistical diagram of grain misorientation (**b, e**), and statistical diagram of KAM value (**c, f**). B&T&D—Before tensile deformation; A&T&D—after tensile deformation; KAM—Kernel average misorientation

The distribution of the grain misorientation diagram in the EBSD of the investigated steel is depicted in Fig. 9, and the statistical diagram and statistical results of grain misorientation are presented in Fig. 8b, e, and Table 2,

respectively. Using the EBSD technology to distinguish the grain boundaries in the selected area, grain misorientation greater than 2° is defined as a grain boundary, that of 2° to 15° is a small-angle grain boundary indicated by red lines,

Table 2 Statistics of EBSD characterization results of investigated steel

Sample	Tensile temperature	Misorientation/%		Mean grain size/ μm	KAM value/($^{\circ}$)
		2 $^{\circ}$ –15 $^{\circ}$	> 15 $^{\circ}$		
A	B&T&D	67.7	32.3	1.1	0.402
	20 $^{\circ}\text{C}$, A&T&D	46.7	53.3	0.7	0.704
	450 $^{\circ}\text{C}$, A&T&D	44.3	55.7	0.5	0.738
B	B&T&D	79.8	20.2	1.3	0.461
	20 $^{\circ}\text{C}$, A&T&D	54.0	46.0	0.5	0.815
	450 $^{\circ}\text{C}$, A&T&D	55.9	44.1	0.6	0.811

**Fig. 9** Grain orientation distribution micrographs for Sample A (a–c) and Sample B (d–f). a, d Before tensile deformation; b, e after tensile deformation at 20 $^{\circ}\text{C}$; c, f after tensile deformation at 450 $^{\circ}\text{C}$

and that greater than 15 $^{\circ}$ is a large-angle grain boundary indicated by black lines. After tensile deformation, the proportion of large-angle grain boundaries increased. Compared to the increase in the proportion of large-angle grain boundaries under the 20 $^{\circ}\text{C}$ tensile test (the proportion of large-angle grain boundaries increased from 32.3% to 53.3% of Sample A and from 20.2% to 46.0% of Sample B), the proportion of large-angle grain boundaries of Sample A increased more significantly under the 450 $^{\circ}\text{C}$ tensile test (the proportion of large-angle grain boundaries increased from 32.3% to 55.7%). The increase in the proportion of large-angle grain boundaries of Sample B is smaller under the 450 $^{\circ}\text{C}$ tensile test (the proportion of large-angle grain boundaries increases from 20.2% to 44.1%). At the same time, compared to Sample A, the

proportion of large-angle grain boundaries in Sample B before and after tensile deformation is lower.

KAM is a method for characterizing local mismatches in the EBSD data analysis. Each KAM value represents the mean deviation angle of the Kikuchi pole between a point and its 24 nearest adjacent points, which can be used to describe strain distribution of the material and calculate the geometrically necessary dislocation density in crystal materials. The KAM distribution diagram, statistical diagram, and statistical results in the investigated steel are presented in Fig. 10, Fig. 8c, f, and Table 2, respectively. The KAM value of the sample increased after tensile deformation. Compared to the increase in KAM value under the 20 $^{\circ}\text{C}$ tensile test (the KAM value increased from 0.402 to 0.704 of Sample A and from 0.461 to 0.815 of Sample B), the increase in KAM value of Sample A was

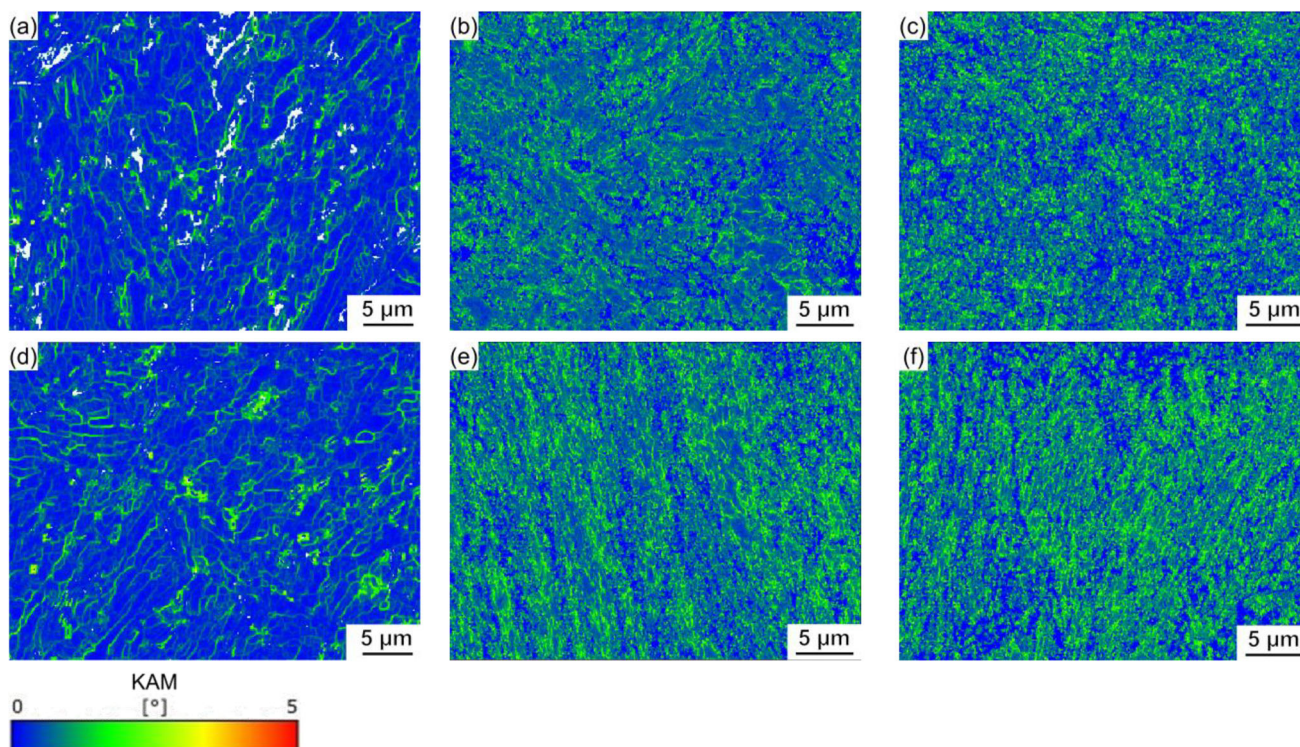


Fig. 10 KAM micrographs for Sample A (a–c) and Sample B (d–f). **a, d** Before tensile deformation; **b, e** after tensile deformation at 20 °C; **c, f** after tensile deformation at 450 °C

greater under the 450 °C tensile test (the KAM value increased from 0.402 to 0.738), the increase in KAM value of Sample B was smaller under the 450 °C tensile test (the KAM value increased from 0.461 to 0.811). Concurrently, compared to Sample A, the KAM values of Sample B before and after tensile deformation are greater.

3.4 Phase volume and carbon content

The XRD diffraction patterns of the investigated steels are illustrated shown in Fig. 11a and b. After tensile deformation of the sample, the diffraction peak of the γ phase

basically disappeared, the intensity of the diffraction peak of $(200)\alpha$ and $(211)\alpha$ slightly decreased, but two new ones were added to the diffraction peak of the α phase ($(112)\alpha$, $(202)\alpha$). In Sample A, compared to the intensity of the α phase diffraction peak under the 20 °C tensile test, the decrease in the intensity of $(200)\alpha$ and $(211)\alpha$ diffraction peak is more significant, and the increase in the intensity of $(112)\alpha$ and $(202)\alpha$ diffraction peak is greater under the 450 °C tensile test.

After calculation, it was found that the retained austenite content and carbon content before and after the tensile deformation are reported in Table 3. The difference in

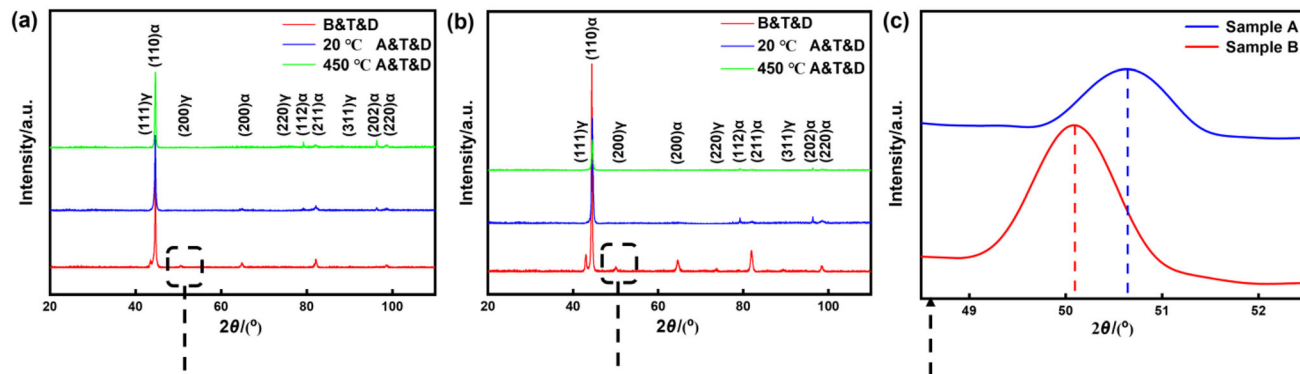


Fig. 11 XRD pattern of investigated steel. **a** Sample A; **b** Sample B; **c** two kinds of untensioned sample partial enlarged diagram of $(200)\gamma$ diffraction peak

Table 3 Quantitative analysis of XRD and EBSD for different phases of investigated steel

Sample	Tensile temperature	V_M /vol.%	V_B /vol.%	V_{RA} /vol.%	C_{RA} /wt.%
A	B&T&D	34.96	54.21	10.83	0.84
	20 °C, A&T&D	45.38	51.47	3.15	1.71
	450 °C, A&T&D	49.47	45.73	4.80	1.34
B	B&T&D	27.83	57.74	14.43	1.60
	20 °C, A&T&D	42.93	53.25	3.82	2.03
	450 °C, A&T&D	47.34	47.88	4.78	1.67

V_M —Volume fraction of martensite; V_B —volume fraction of bainite; V_{RA} —volume fraction of retained austenite; C_{RA} —carbon content of retained austenite

retained austenite content between Sample A (10.83 vol.%) and Sample B (14.43 vol.%) is very small, but the difference in carbon content between the two is significant. The carbon content of the retained austenite in the former is almost half that in the latter because the carbon enrichment time of austenite of Sample B is longer, the content of the BCC phase (bainite and martensite) of carbon discharge to austenite is higher, and the austenite size is smaller, and the propagation distance is shorter. This is consistent with the results presented in Fig. 11c (compared to Sample B, the (111) γ diffraction peak of Sample A shifts significantly to the right). The retained austenite content significantly decreased, and the carbon content increased in the sample after tensile deformation. Compared to room temperature stretching, the change in retained austenite carbon content under high-temperature stretching is smaller. After 20 °C stretching, the carbon content of retained austenite increases from 0.84 to 1.71 wt.% of Sample A, and the carbon content of retained austenite increases from 1.60 to 2.03 wt.% of Sample B. After 450 °C stretching, the carbon content of retained austenite increases from 0.84 to 1.34 wt.% in Sample A, and the carbon content of retained austenite increases from 1.60 to 1.67 wt.% in Sample B. This is due to the migration of carbon elements in the sample at high temperatures [39] and the decomposition of carbon-rich austenite, resulting in the decrease in carbon content in retained austenite.

Due to the complexity of the microstructure of bainite after isothermal transformation, the energy band comparison results are obtained by EBSD, and the body-centered cubic phase is analyzed (Figs. 12 and 13). Based on the Kikuchi model of band contrast (BC), the distributions of martensite and bainite–ferrite fraction are analyzed using the BC data and the Gaussian multiple peak fitting method [40–42] (Fig. 12). Compared with martensite, the lattice defect density of bainitic–ferrite is lower, i.e., bainitic–ferrite has a strong band contrast in the BC diagram [40]. The difference between martensite and bainitic–ferrite in the BC

diagram needs to be distinguished, which can be achieved by defining a threshold in the Gaussian diagram. Thus, the intersection point of the Gaussian curve is set as the threshold value. Due to the proximity of the EBSD scanning step length to the width of film RA, it is difficult to detect film retained austenite. Thus, the volume fraction of retained austenite displayed by the EBSD is less than the actual situation, most of which block RA. Note that the EBSD volume fraction statistics are only employed as semi-quantitative results to study the distribution of phase positions and the changes in phase proportions before and after tensile deformation. The retained austenite volume fraction data are still based on the XRD calculation results.

The statistical results of the contents of retained austenite, bainite and martensite phases before and after tensile deformation are reported in Table 3. Before tensile deformation, the proportion of hard phase structure is relatively high in Sample A. The martensite content is 34.96 vol.%, the proportion of bainite is 54.21 vol.%, and the retained austenite is 10.83 vol.%. The proportion of hard phase structure is relatively low in Sample B. The martensite content is 27.83 vol.%, the proportion of bainite is 57.74 vol.%, and the retained austenite is 14.43 vol.%. The martensite content of Sample A is higher than that of Sample B. This is due to the fact that the bainite isothermal time of Sample A is short, the transformation from the original austenite to bainite is insufficient, the bainite isothermal temperature is higher than the M_s temperature and the cooling time is longer. The high proportion of hard phase and the martensite content is the important factors that cause the high tensile strength of Sample A and the significant decrease in tensile strength at high temperatures. After tensile deformation, the proportion of retained austenite decreases, the proportion of martensite increases, and the block retained austenite disappears, which is consistent with the results presented in Fig. 4. The phase distribution diagram also shows that the content of block retained austenite is lower in Sample B.

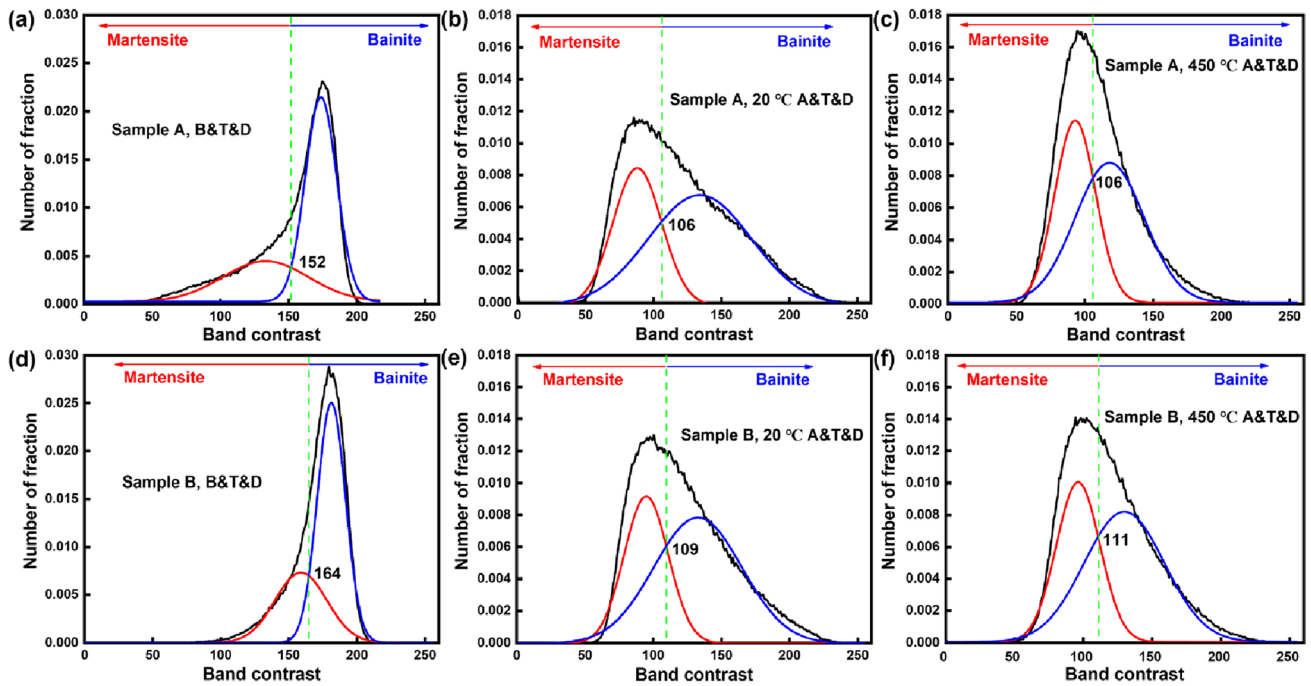


Fig. 12 Gaussian-fitting diagram of BC value. **a, d** Before tensile deformation; **b, e** after tensile deformation at 20 °C; **c, f** after tensile deformation at 450 °C

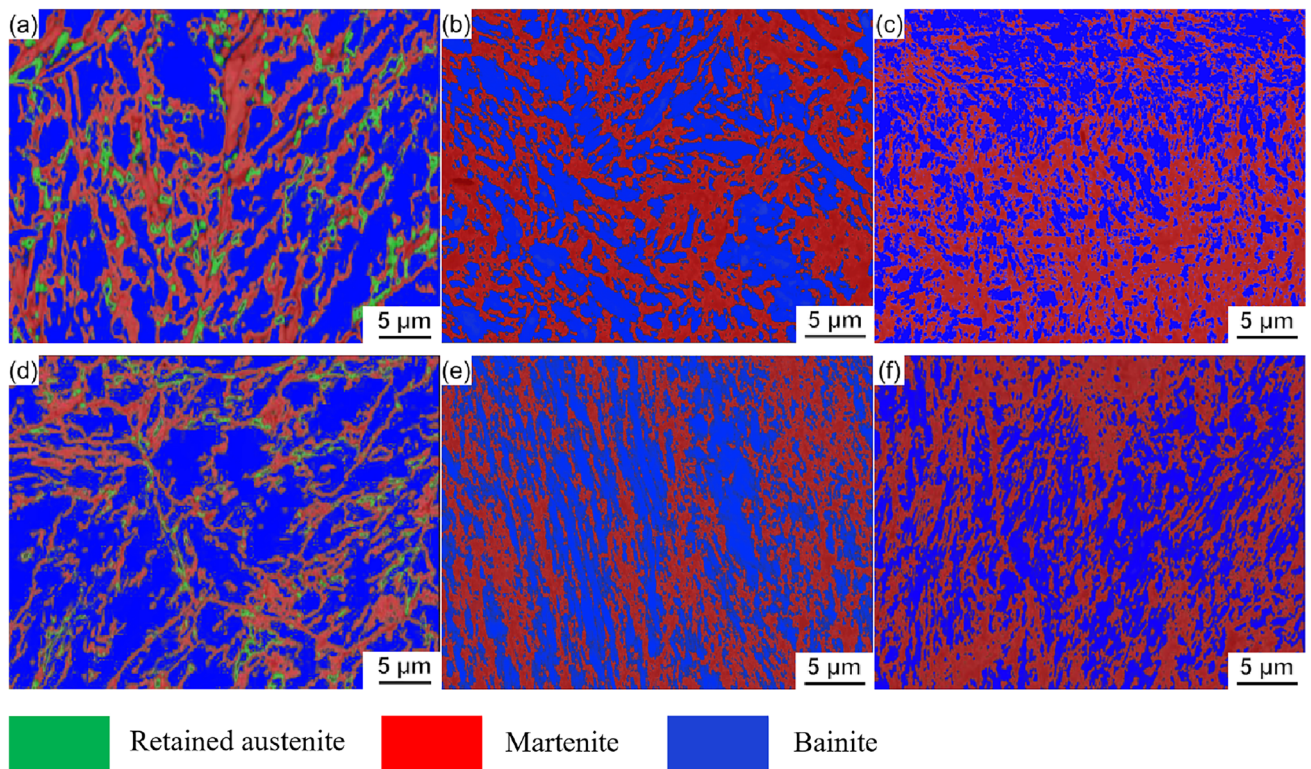


Fig. 13 Phase distribution diagram of Sample A (**a–c**) and Sample B (**d–f**). **a, d** Before tensile deformation; **b, e** after tensile deformation at 20 °C; **c, f** after tensile deformation at 450 °C

4 Discussion

4.1 Work-hardening behavior

Three flow stress models were selected to simulate the tensile curves of two sample types (Fig. 14). The first one was the Hollomon model (Eqs. (8) and (9)), which has been widely used to reflect the change of strain hardening index in the stress–strain curve and is suitable for the whole tensile stage. The second model is the Crussard–Jaoul (C–J) model (Eqs. (10) and (11)), which reflects not only the work-hardening performance of metals but also the changes in the work-hardening mechanisms at different deformation stages. It should be noted that the modified C–J model (Eqs. (12) and (13)) is more suitable for analyzing the strain-hardening behavior of multiphase steel. Although the C–J and modified C–J models only apply to the uniform elongation stages, the modified C–J model is more sensitive to microstructure change, and it best describes the working hardening behavior of carbide-free bainitic steel [43, 44].

$$\sigma = k_H \varepsilon^{n_H} \tag{8}$$

$$\ln \sigma = n_H \ln \varepsilon + \ln k_H \tag{9}$$

$$\sigma = \sigma_0 + k_L \varepsilon^{n_L} \tag{10}$$

$$\ln \left(\frac{d\sigma}{d\varepsilon} \right) = (n_L - 1) \ln \varepsilon + \ln(k_L n_L) \tag{11}$$

$$\varepsilon = \varepsilon_0 + k_S \sigma^{n_S} \tag{12}$$

$$\ln \left(\frac{d\sigma}{d\varepsilon} \right) = (1 - n_S) \ln \sigma - \ln(k_S n_S) \tag{13}$$

where σ and ε are true stress and true strain; n is the corresponding strain-hardening exponent (H-HM model, L–C–J model, S-modify C–J model); and $\varepsilon_0, k, \sigma_0$ are material constants. The Hollomon model represents the existence of multiple strain-hardening mechanisms during the deformation process. The deformation process of the C–J and the modified C–J models can be divided into three stages, and the slope and turning strain points of each stage are listed in Table 4. The transformation of retained austenite corresponds to the second stage. After a certain degree of plastic deformation due to low mechanical stability, the block retained austenite takes the lead in the strain-induced martensitic transformation, forming high-hardness martensite and improving the strain-hardening ability of materials [45, 46].

Two types of steels underwent three stages during the tensile process at different temperatures: elastic deformation (I), plastic deformation (II) and necking fracture (III). In the first stage, the soft phase deformed. Specifically, first, the retained austenite stress was concentrated, a uniform deformation and a dislocation slip occurred,

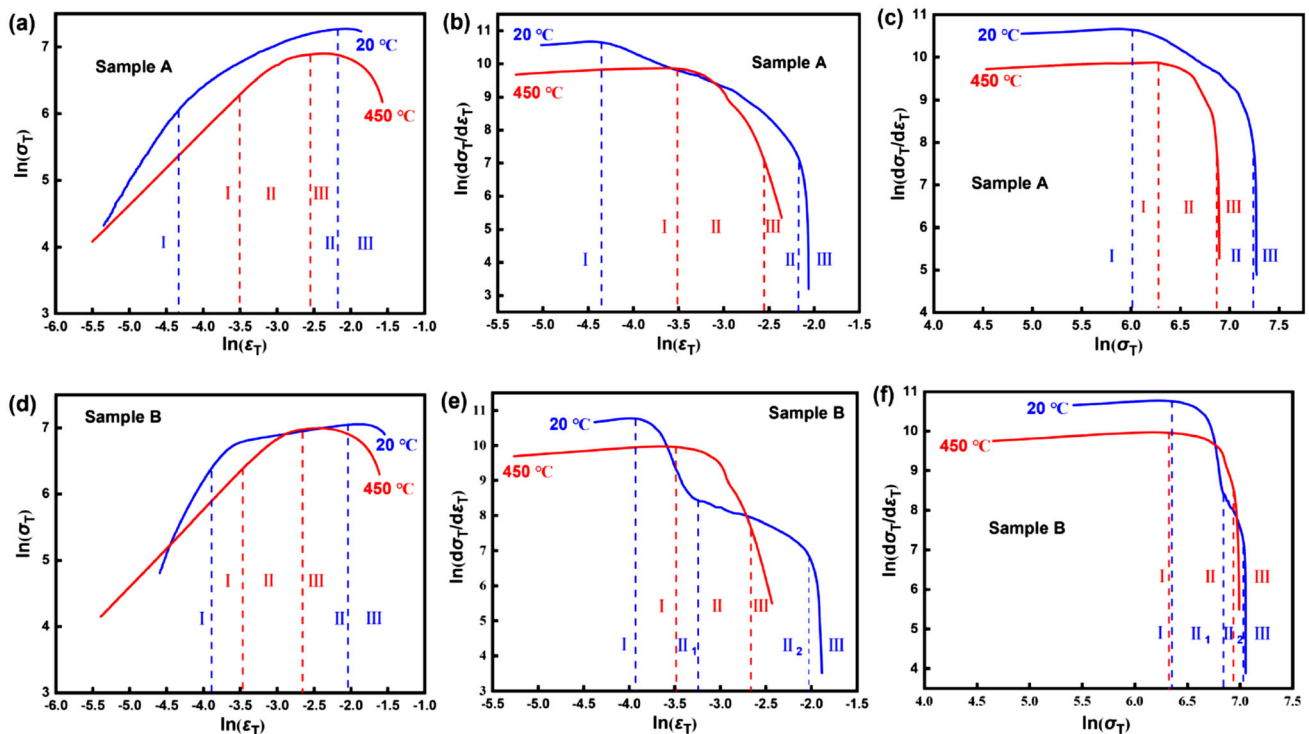


Fig. 14 Hollomon analysis (a, d), C–J analysis (b, e), and modified C–J analysis (c, f) of investigated steel

Table 4 Slope and turning strain points for each stage of three simulation models

Hollomon analysis						
Sample	Tensile temperature/°C	Slope (n)			ε_T	
		I	II	III	Stage I to II	Stage II to III
A	20	1.70	0.51	− 0.09	0.013	0.113
	450	1.11	0.66	− 0.64	0.030	0.078
B	20	2.16	0.23	− 0.25	0.020	0.131
	450	1.17	0.79	− 0.58	0.031	0.070
C–J analysis						
Sample	Tensile temperature/°C	Slope ($n_L - 1$)			ε_T	
		I	II	III	Stage I to II	Stage II to III
A	20	0.16	− 1.44	− 22.17	0.013	0.113
	450	0.10	− 2.66	− 8.99	0.030	0.078
B	20	0.26	− 1.75	− 18.78	0.020	0.131
	450	0.16	− 2.42	− 9.36	0.031	0.070
Modified C–J analysis						
Sample	Tensile temperature/°C	Slope ($1 - n_S$)			ε_T	
		I	II	III	Stage I to II	Stage II to III
A	20	0.11	− 2.07	− 66.10	0.013	0.095
	450	0.084	− 2.99	− 92.99	0.030	0.068
B	20	0.13	− 6.97	− 85.86	0.020	0.117
	450	0.14	− 1.69	− 51.78	0.031	0.066

providing potential nucleation sites for subsequent martensite transformation and promoting martensite transformation, while the strain-hardening index was unchanged. Compared to the first stage during the room temperature tensile process, the strain change during the first stage under the high-temperature tensile process was greater due to the decrease in hard phase hardness in the sample at high temperatures. The strain-hardening index continuously changed during the second stage and retained austenite underwent martensite transformation. At room temperature, as the tensile process progressed, the martensite transformation first occurred in the block retained austenite with low stability, forming hard martensite, generating volume expansion, alleviating stress concentration and crack growth, and effectively improving the strength and plasticity of the sample. At the end of the second stage, the block retained austenite was basically depleted, and some of the film retained austenite underwent strain-induced martensite transformation. Since the film retained austenite had a high carbon content and low transformation driving force, it required greater external strain to make it undergo martensite transformation, and its size was small with fewer nucleation sites. The surrounding

bainite–ferrite laths prevented martensite shear transformation. Thus, the film retained austenite is difficult to undergo martensite transformation.

Compared to the second stage during the room temperature tensile process, the second stage during the high-temperature tensile process was shorter, and the strain-hardening index was higher. Among them, the strain-hardening index during the plastic deformation stage of Sample B at high temperatures was the highest because the driving force for retained austenite phase transformation decreased at high temperatures, while the driving force of low-carbon retained austenite phase transformation was greater and low-carbon retained austenite was easier to transform. The retained austenite of Sample B decomposed at high temperatures and the carbon content was significantly reduced. Hence, the transformation amount of retained austenite decreased, and the transformation rate increased. For the transformation situation, the poor-carbon block retained austenite underwent martensite transformation first, and after the transformation was completed, the low-carbon film retained austenite underwent martensite transformation. The room temperature tensile simulation curve of Sample B demonstrates an obvious inflection

point in the second stage. Since its retained austenite had a high carbon content, after the sample yields, there was no rapid martensite transformation. Hence, the retained austenite slowly underwent martensite transformation only after sufficient external strain. The rich-carbon retained austenite underwent martensite transformation, which significantly improved the plasticity, and the strength improvement was relatively small. The necking fracture stage was a mixed deformation of bainite–ferrite, martensite, and retained austenite. All structures underwent plastic deformation together, and the deformation of microstructure components and the accumulation of dislocations at phase boundaries resulted in high slopes.

4.2 Plastic deformation mechanism

The chemical driving force for the transformation of retained austenite ΔG^{chem} is provided by undercooling, which decreases as the temperature increases. The temperature at which the chemical driving force is zero is called the thermodynamic equilibrium temperature (T_{OM}) of austenite–martensite two-phases. Martensitic transformation occurs only when the thermodynamic conditions of Eq. (14) are satisfied without the influence of external force. The mechanical driving force ΔG^{mech} is provided by an external force. When the temperature is higher than M'_s , the chemical driving force is insufficient to support the transformation of retained austenite, and external stress is required to drive the retained austenite to undergo martensite transformation. Equation (15) is the thermodynamic condition of martensite transformation under the action of an external force. In order to explore the transformation thermodynamic differences of two isothermal bainitic steels at different temperatures, the Gibbs free energy function of retained austenite and martensite with temperature was used to explain the different stages of stress-induced martensite transformation and strain-induced martensite transformation of retained austenite [47].

$$\Delta G^{\text{RA} \rightarrow \text{M}} = \Delta G^{\text{chem}} < G_{\text{N}}^{\text{M}} + E_{\text{str}} \tag{14}$$

$$\Delta G^{\text{RA} \rightarrow \text{M}} = \Delta G^{\text{chem}} + \Delta G^{\text{mech}} < G_{\text{N}}^{\text{M}} + E_{\text{str}} \tag{15}$$

$$\Delta G^{\gamma \rightarrow \alpha'} = G^{\gamma} - G^{\alpha'} = \Delta G^{M_s} + \Delta S^{M_s}(T - M_s) \tag{16}$$

$$\Delta G^{\gamma \rightarrow \alpha'} = (1 - x)\Delta G_{\text{Fe}}^{\gamma \rightarrow \alpha'} + x\Delta H^{\gamma \rightarrow \alpha'} \tag{17}$$

$$M'_s = 550 - 240w_{\text{C}} - 45w_{\text{Mn}} - 35w_{\text{Cr}} - 26w_{\text{Ni}} - 25w_{\text{Mo}} - 30w_{\text{V}} - 7w_{\text{Cu}} - 0w_{\text{Si}} + 12w_{\text{Co}} + 13w_{\text{Al}} \tag{18}$$

where $\Delta G^{\text{RA} \rightarrow \text{M}}$ is the total free energy difference from retained austenite to martensite when there is no

composition change; G_{N}^{M} is the critical driving force required for martensite trimming transformation; E_{str} is the storage energy of martensite, 600 J/mol; $\Delta G^{\gamma \rightarrow \alpha'}$ is the Gibbs free energy difference between retained austenite and α' -martensite; G^{γ} and $G^{\alpha'}$ is the Gibbs free energy of retained austenite and α' -martensite, respectively; T is the absolute temperature; and ΔG^{M_s} and ΔS^{M_s} are the chemical driving force and the entropy difference between the austenite and martensite at the M_s temperature, respectively; x is the element contents, at.%; and $\Delta H^{\gamma \rightarrow \alpha'}$ is heat liberated by austenite-to-martensite reaction, J/mol; $\Delta G_{\text{Fe}}^{\gamma \rightarrow \alpha'}$ the difference in free energy between face-centered cubic (FCC) and BCC iron, J/mol; and w_i is the mass fraction of alloy element i .

Figure 15 illustrates the curves of the mechanical and chemical driving forces that change with temperature, where M'_{sA} and M'_{sB} are the starting temperature of martensite transformation of retained austenite in Samples A and B, respectively. At this temperature, the transformation driving force provided by the chemical driving force is equal to the critical driving force of martensite transformation (i.e., $\Delta G^{\text{RA} \rightarrow \text{M}} = \Delta G_{M'_s}^{\text{chem}} = G_{\text{N}}^{\text{M}} + E_{\text{str}}$). When the temperature exceeds M'_s or is less than T_{OM} , the transformation driving force provided by the chemical driving force is less than the critical driving force required for martensite transformation. Only by increasing the mechanical driving force to achieve the critical driving force (i.e., $\Delta G^{\text{RA} \rightarrow \text{M}} = \Delta G_T^{\text{chem}} + \Delta G_T^{\text{mech}} = \Delta G_{M'_s}^{\text{RA} \rightarrow \text{M}} = G_{\text{N}}^{\text{M}} + E_{\text{str}}$) of martensite transformation, martensite transformation can occur. When the temperature is between M'_{sA} and M_{sA}^{σ} or between M'_{sB} and M_{sB}^{σ} (M_{sA}^{σ} and M_{sB}^{σ} is the upper limit temperature of stress-induced martensite phase transformation of Samples A and B, respectively), the elastic stress produced by maintaining the martensite transformation is called the stress-induced transformation stage. When the temperature is higher than M_{sA}^{σ} and M_{sB}^{σ} , the elastic stress can no longer provide enough mechanical driving force. Therefore, the required stress must be higher than the yield strength of the retained austenite, i.e., only plastic deformation of the retained austenite can occur in this case. Hence, the strain-induced martensite transformation occurs in $M_{sA}^{\sigma} - M_{dA}$ or $M_{sB}^{\sigma} - M_{dB}$ the stages. When the temperature exceeds M_{dA} and M_{dB} (M_{dA} and M_{dB} is the upper limit temperature of strain-induced martensite phase transformation of Samples A and B, respectively), the plastic deformation cannot provide enough mechanical driving force for the retained austenite to cause martensite transformation, so that the retained austenite only deforms at this stage without transformation [48, 49].

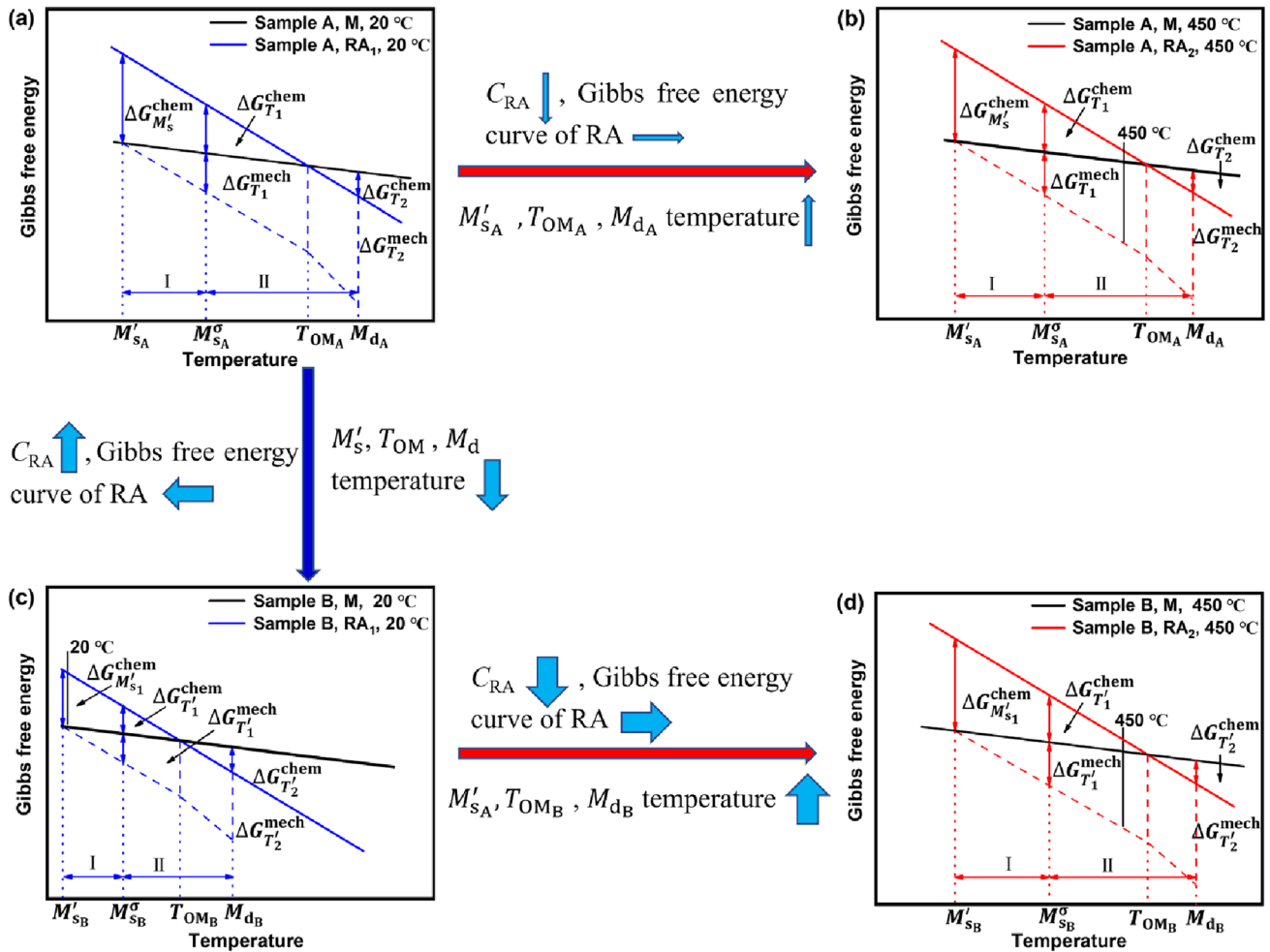


Fig. 15 Mechanical and chemical driving forces curves with temperature. **a, c** After 20 °C tensile deformation; **b, d** after 450 °C tensile deformation. I and II represent stress and strain-induced phase transformation, respectively

According to Refs. [24, 25], the stability of retained austenite is influenced by temperature, chemical composition, grain size/morphology, and stress state. Among them, temperature is the most important factor affecting austenite stability, where $\Delta G^{\gamma \rightarrow \alpha'}$ decreases with the increase in temperature (Eq. (16) [25, 49, 50]). The second is chemical elements, which can be improved by increasing the content of C, N, Mn, and Ni. The effect of the carbon element is most significant, which can be estimated using Eq. (17) [51].

There is a significant difference in the carbon content of retained austenite between Samples A and B, resulting in a significant difference in M'_s and $\Delta G^{\gamma \rightarrow \alpha'}$. The retained austenite in Sample A has a low carbon content and high chemical driving force and is prone to phase transformation; the M'_{SA} temperature is higher than 20 °C. The retained austenite of Sample B has high carbon content, small size, small chemical driving force, and an M'_{SB} temperature lower than 20 °C. Thus, it needs to provide more

mechanical force for martensite transformation. The martensite in the sample after tensile at room temperature includes pre-martensite, transformation-induced martensite, and martensite formed during cooling.

The carbon content of the retained austenite is low in Sample A, the thermal stability is high, and no decomposition occurs at high temperatures. However, the martensite in the sample decomposes (Fig. 16a), the carbon element migrates, and the carbon content of the retained austenite decreases slightly. Therefore, the Gibbs free energy curve of the retained austenite shifts slightly to the right and M'_{SA} , T_{OMA} , and M_{dA} rise slightly, but the deformation temperature is higher than M'_{SA} and lower than T_{OMA} (the thermodynamic equilibrium temperature of austenite–martensite two-phases in Sample A), and $\Delta G^{\gamma \rightarrow \alpha'}$ significantly decreases. Hence, martensite transformation is difficult to occur. The retained austenite in Sample B has a high carbon content and poor thermal stability. It decomposes at high temperatures (Fig. 16b), producing fine

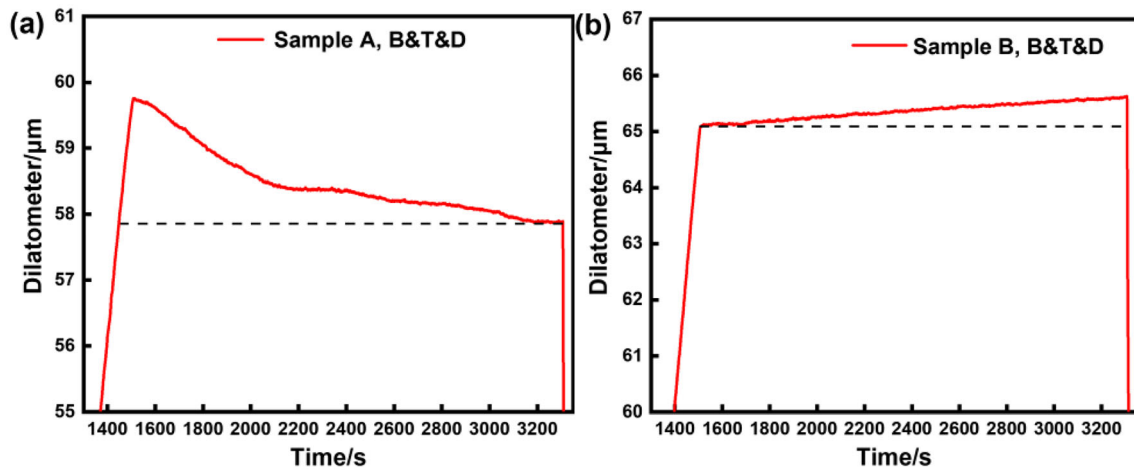


Fig. 16 Thermal expansion curves of investigated steels during 450 °C heat preservation. **a** Sample A; **b** Sample B

cementite and ferrite. The carbon content of the retained austenite significantly decreases. Accordingly, the Gibbs free energy curve of the retained austenite shifts significantly to the right, and M'_{SB} , T_{OMB} , and M_{dB} significantly increase. The deformation temperature is higher than M'_{SB} but lower than T_{OMB} (the thermodynamic equilibrium temperature of austenite–martensite two-phases in Sample B), and M'_{SB} is higher than 20 °C. With the increase in tensile temperature and the decrease in the retained austenite carbon content, $\Delta G^{\gamma \rightarrow \alpha'}$ significantly decreases and the transformation rate increases. Thus, only a small amount of retained austenite in the samples undergoes martensite transformation at high temperatures, and some retained austenite undergoes martensite transformation during cooling after tensile deformation. There are two more types of martensite in the sample after high-temperature tension than after room temperature tension, i.e., tempered martensite and martensite formed during cooling after tensile deformation. Since martensite in Sample A decomposes at high temperatures, the hardness decreases significantly, and only a small amount of retained austenite produces the TRIP effect, leading to a significant decrease in its tensile strength.

5 Conclusions

1. Compared with the mechanical properties at room temperature, the uniform elongation of investigated steel at high temperatures significantly decreased (the uniform elongation of the sample austempered above M_s decreased from 8.0% to 3.5%, and that below M_s decreased from 10.9% to 3.1%). The change in tensile strength of the two kinds of bainitic steels was significantly different (the tensile strength of the sample
2. The carbon element of the sample migrated at high temperatures, the carbon-rich retained austenite decomposed, and the carbon content of retained austenite decreased. In the process of high-temperature tension, the content of retained austenite-to-martensitic transformation decreased, the martensite decomposed, the hard phase softened, and the tensile strength of the sample decreased.
3. The sample austempered below M_s had a high carbon content of retained austenite, a high proportion of film retained austenite, high mechanical stability, and low thermal stability. The retained austenite decomposed at high temperatures, and the carbon content remarkably decreased. During the tensile process, the phase change content decreased and the phase change rate accelerated.
4. The sample austempered above M_s had a low carbon content of retained austenite, a high proportion of block retained austenite, and low mechanical stability and high thermal stability. The martensitic transformation was difficult to occur at high temperature, as only a part of low carbon retained austenite occurred during martensitic transformation, where the martensite decomposed, and the strength and uniform elongation of the sample decreased.
5. During the high-temperature tensile process, the TRIP effect of the sample was weak. Combined with the flow stress-strain model analysis, it was found that the plastic deformation ability of the sample weakened, the transformation rate of retained austenite increased, the work hardening index of the sample increased, and necking was obvious. When the carbon content of

retained austenite in the sample is high, its stability will undergo significant changes at high temperatures.

Acknowledgements The authors gratefully acknowledge the financial support from the National Natural Science Foundation of China (52071238), Leading Innovation and Entrepreneurship Team in Zhejiang Province (2021R01020), the Key Research and Development Program of Hubei Province (2021BAA057), Science and Technology Program of Guangxi Province (AA22068080), and the 111 Project. The authors show thanks for the technical support provided by Analysis and Test Center of Wuhan University of Science and Technology.

Declarations

Conflicts of interest The authors declare that they have no known competing financial interests or personal relationships that could have appeared to influence the work reported in this paper.

References

- [1] Z. Yang, F. Zhang, *ISIJ Int.* 60 (2020) 18–30.
- [2] T. Sourmail, F.G. Caballero, C. Garcia-Mateo, V. Smanio, C. Ziegler, M. Kuntz, R. Elvira, A. Leiro, E. Vuorinen, T. Teeri, *Mater. Sci. Technol.* 29 (2013) 1166–1173.
- [3] A. Królicka, A.M. Žak, F.G. Caballero, *Mater. Des.* 211 (2021) 110143.
- [4] M. Kuntz, C. Garcia-Mateo, F.G. Caballero, V. Ruiz-Jimenez, T. Sourmail, S. Lille, G. Wicks, S. Allain, S. Denis, G. Geandier, in: European Commission Directorate G-Industrial Technologies, Unit, G.5-Research Fund for Coal and Steel, 2020, pp. 754070.
- [5] K. Wang, X. Gui, B. Bai, G. Gao, *Mater. Sci. Eng. A* 850 (2022) 143525.
- [6] X. Wang, X. Zhang, Q. Fang, H. Ma, R. Zhang, F. Liu, Z. Yang, F. Zhang, *Mater. Sci. Eng. A* 856 (2022) 143958.
- [7] X. Long, G. Zhao, F. Zhang, S. Xu, Z. Yang, G. Du, R. Branco, *Mater. Sci. Eng. A* 775 (2020) 138964.
- [8] G.M.A.M. El Fallah, H.K.D.H. Bhadeshia, *Mater. Sci. Eng. A* 746 (2019) 145–153.
- [9] R. Kumar, R.K. Dwivedi, S. Ahmed, *Silicon* 13 (2021) 1249–1259.
- [10] K. Wang, F. Hu, S. Zhou, O. Isayev, S. Yershov, Z. Zhang, K. Wu, *Mater. Lett.* 324 (2022) 132517.
- [11] F.D. Fischer, G. Reisner, E. Werner, K. Tanaka, G. Cailletaud, T. Antretter, *Int. J. Plast.* 16 (2000) 723–748.
- [12] W. Bleck, X. Guo, Y. Ma, *Steel Res. Int.* 88 (2017) 1700218.
- [13] H.K.D.H. Bhadeshia, IOM communications, London, UK, 2015.
- [14] E.V. Pereloma, I.B. Timokhina, M.K. Miller, P.D. Hodgson, *Acta Mater.* 55 (2007) 2587–2598.
- [15] I.B. Timokhina, P.D. Hodgson, E.V. Pereloma, *Metall. Mater. Trans. A* 35 (2004) 2331–2341.
- [16] D.P. Koistinen, R.E. Marburger, *Acta Metall.* 7 (1959) 59–60.
- [17] C.K. Syn, B. Fultz, J.W. Morris, *Metall. Trans. A* 9 (1978) 1635–1640.
- [18] M. Izumiyama, M. Tsuchiya, Y. Imai, *Jpn. Inst. Met. Mater.* 34 (1970) 291–295.
- [19] J. Huang, Z. Xu, *Mater. Sci. Eng. A* 438–440 (2006) 254–257.
- [20] P.J. Brofman, G.S. Ansell, *Metall. Trans. A* 14 (1983) 1929–1931.
- [21] S. Lee, S.J. Lee, B.C. De Cooman, *Scripta Mater.* 65 (2011) 225–228.
- [22] A. Eres-Castellanos, F.G. Caballero, C. Garcia-Mateo, *Acta Mater.* 189 (2020) 60–72.
- [23] Y. Mine, K. Hirashita, H. Takashima, M. Matsuda, K. Takashima, *Mater. Sci. Eng. A* 560 (2013) 535–544.
- [24] B.B. He, *Materials* 13 (2020) E3400.
- [25] Y. Li, D.S. Martín, J.L. Wang, C.C. Wang, W. Xu, *J. Mater. Sci. Technol.* 91 (2021) 200–214.
- [26] V. Ruiz-Jimenez, M. Kuntz, T. Sourmail, F.G. Caballero, J.A. Jimenez, C. Garcia-Mateo, *Appl. Sci.* 10 (2020) 8901.
- [27] C. Garcia-Mateo, M. Peet, F.G. Caballero, H.K.D.H. Bhadeshia, *Mater. Sci. Technol.* 20 (2004) 814–818.
- [28] A. Saha Podder, H.K.D.H. Bhadeshia, *Mater. Sci. Eng. A* 527 (2010) 2121–2128.
- [29] A. Saha Podder, *Tempering of a mixture of bainite and retained austenite*, University of Cambridge, Cambridge, UK, 2011.
- [30] I.B. Timokhina, H. Beladi, X.Y. Xiong, Y. Adachi, P.D. Hodgson, *Acta Mater.* 59 (2011) 5511–5522.
- [31] F.G. Caballero, M.K. Miller, S.S. Babu, C. Garcia-Mateo, *Acta Mater.* 55 (2007) 381–390.
- [32] F.G. Caballero, M.K. Miller, C. Garcia-Mateo, *Acta Mater.* 58 (2010) 2338–2343.
- [33] S.B. Zhou, C.Y. Hu, F. Hu, L. Cheng, O. Isayev, S. Yershov, H.J. Xiang, K.M. Wu, *Mater. Sci. Eng. A* 846 (2022) 143175.
- [34] S.B. Zhou, F. Hu, W. Zhou, L. Cheng, C.Y. Hu, K.M. Wu, *J. Mater. Res. Technol.* 14 (2021) 1021–1034.
- [35] T. He, L. Wang, F. Hu, W. Zhou, Z. Zhang, K. Wu, *J. Mater. Res. Technol.* 22 (2023) 2690–2703.
- [36] A.K. De, D.C. Murdock, M.C. Mataya, J.G. Speer, D.K. Matlock, *Scripta Mater.* 50 (2004) 1445–1449.
- [37] S.W. Young, M. Sato, K. Yamamitsu, Y. Shimada, Y. Zhang, G. Miyamoto, T. Furuhashi, *Acta Mater.* 206 (2021) 116612.
- [38] X.P. Yu, H.B. Wu, Y. Gu, R. Yuan, Y.Y. Zhang, Y.H. Feng, *J. Iron Steel Res. Int.* 29 (2022) 647–654.
- [39] F. Zhu, F. Chai, X.B. Luo, Z.Y. Zhang, C.F. Yang, *J. Iron Steel Res. Int.* 28 (2021) 464–478.
- [40] K. Chen, H.B. Li, Z.H. Jiang, F.B. Liu, C.P. Kang, X.D. Ma, *J. Mater. Sci. Technol.* 72 (2021) 81–92.
- [41] M.S. Baek, K.S. Kim, T.W. Park, J. Ham, K.A. Lee, *Mater. Sci. Eng. A* 785 (2020) 139375.
- [42] S. Breumier, T. Martinez Ostormujof, B. Frincu, N. Gey, A. Couturier, N. Loukachenko, P.E. Aba-perea, L. Germain, *Mater. Charact.* 186 (2022) 111805.
- [43] S. Das, S. Sinha, A. Lodh, A.R. Chintha, M. Krugla, A. Haldar, *Mater. Sci. Technol.* 33 (2017) 1026–1037.
- [44] Y.I. Son, Y.K. Lee, K.T. Park, C.S. Lee, D.H. Shin, *Acta Mater.* 53 (2005) 3125–3134.
- [45] S.M. Hasan, A. Mandal, S.B. Singh, D. Chakrabarti, *Mater. Sci. Eng. A* 751 (2019) 142–153.
- [46] J. Hu, X. Li, Q. Meng, L. Wang, Y. Li, W. Xu, *Mater. Sci. Eng. A* 855 (2022) 143904.
- [47] M. Mukherjee, S.B. Singh, O.N. Mohanty, *Metall. Mater. Trans. A* 39 (2008) 2319–2328.
- [48] J. Wang, S. Zwaag, *Metall. Mater. Trans. A* 32 (2001) 1527–1539.
- [49] K. Ishida, *Scripta Metall.* 11 (1977) 237–242.
- [50] A. Perlade, O. Bouaziz, Q. Furnémont, *Mater. Sci. Eng. A* 356 (2003) 145–152.
- [51] L. Kaufman, M. Cohen, *Prog. Met. Phys.* 7 (1958) 165–246.

Springer Nature or its licensor (e.g. a society or other partner) holds exclusive rights to this article under a publishing agreement with the author(s) or other rightsholder(s); author self-archiving of the accepted manuscript version of this article is solely governed by the terms of such publishing agreement and applicable law.